4 Oxide Heterostructure Project

– Observation and control of novel quantum phenomena in superstructures of strongly correlated oxides –

Project Leader: Hiroshi KUMIGASHIRA

4-1 Introduction

The goal of this project is to design novel physical properties appearing at the heterointerface of strongly correlated oxides. The physical properties arise from strong mutual coupling among the spin, charge, and orbital degrees of freedom in the interface region between two different oxides [1]. In order to control such properties, it is necessary to clarify the interfacial electronic, magnetic, and orbital structures. We are therefore using synchrotron radiation spectroscopic techniques having elemental selectivity to probe these structures in the nm-scale at the oxide heterointerface. For example, the electronic structure at the interface is determined by photoemission spectroscopy (PES) and X-ray absorption spectroscopy (XAS), the magnetic structure by magnetic circular dichroism of XAS, and the orbital structure by linear dichroism of XAS. We aim to design and create novel quantum materials by optimally combining sophisticated oxide growth techniques using laser molecular beam epitaxy (MBE) and advanced analysis techniques using quantum beams.

4-2 Construction of new beamline for surface and interface studies of oxide superstructures

We have designed and constructed a new undulator beamline MUSASHI (Multiple Undulator beamline for Spectroscopic Analysis on Surface and HeteroInterface) at the BL-2 section of the PF-ring (Fig. 1). This new beamline has two types of undulator in tandem alignment; one is designed for the vacuum ultraviolet (VUV) region (30–300 eV), and the other for the soft X-ray (SX) region (250–2000 eV). Consequently, relatively wide energy-range light while maintaining both high brilliance and high energy resolution will be available in this beamline by the combination of the two undulators and a variable-included-angle varied-line-spacing plane-grating (VLSPG) monochromator. Moreover, an additional double-crystal monochromator is built into this branch beamline (BL-2B) to have the energy range of 2000–4000 eV available using the wiggler mode of the SX undulator. Our developed system "*in-situ* photoelectron spectrometer – laser MBE" will be installed at the new beamline BL-2A as an endstation (Fig. 2).

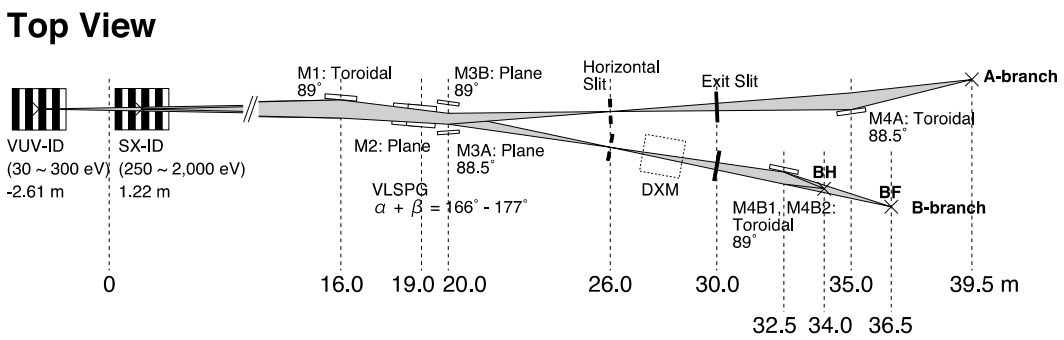

Fig. 1: Layout of new BL-2 "MUSASHI".

The performance of the new beamline in terms of energy resolution has been evaluated for SX and VUV mode. Figure 3(a) shows a photoabsorption spectrum of N_2 molecules obtained using the new beamline optics with SX undulator light. The fitting result by Voigt functions with Gaussian width of 29 meV and the Lorentzian width of 117 meV indicates that a resolving power (E/ΔE) of much more than 10,000 is achieved for the SX optics of the new BL-2 beamline. Moreover, the photon flux at the endstation is more than 10^{12} photons/sec at the energy resolution of E/ΔE ~ 10,000. The performances are much better than that of the previous BL-2C beamline [2]. For VUV mode, the resolving power is evaluated by measuring a photoionization spectrum of double excited He obtained as shown in Fig. 3(b). The narrowest peak width of 3.0 meV in the $(2,0)_{18}$ resonance peak is obtained, indicating that a resolving power of more than 20,000 is achieved from the VUV optics of the new BL-2 beamline. This resolving power is comparable to that of the VUV undulator beamline BL-28 at PF [3].

Previously, we had mainly used the *in-situ* PES – laser MBE system either at the BL-28 for angle-resolved photoemission spectroscopy (ARPES) in the VUV region or at the old BL-2C for photoemission spectroscopy and X-ray absorption spectroscopy in the SX region. However, at the new BL-2A, we will perform both VUV and SX spectroscopic measurements at the same time, for the same grown sample, with the same experimental setup. This approach guarantees the quality of the experimental data, and offers numerous benefits to the field of surface science: the newly developed system enables us to obtain complete information

Fig. 2: Photo of the developed in-situ ARPES – laser MBE system installed at the MUSASHI beamline.

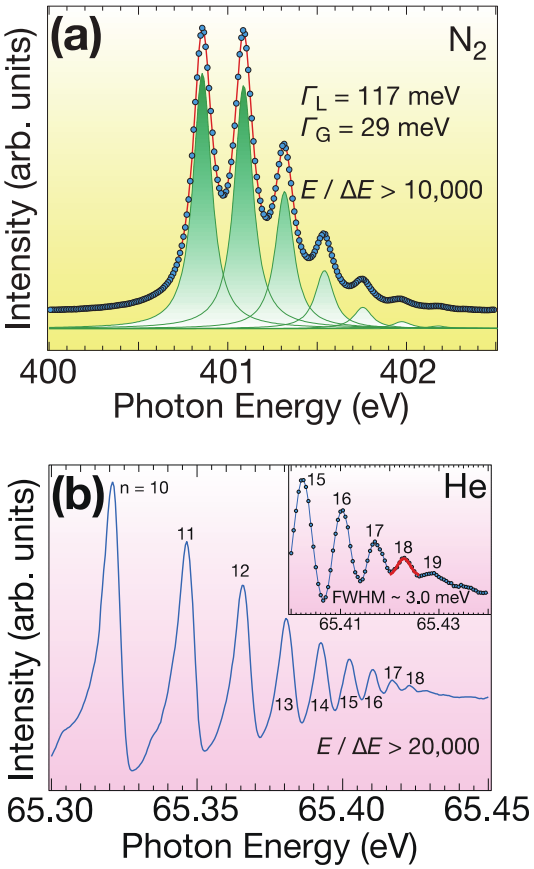

Fig. 3: (a) $1s\sigma \rightarrow \pi^*$ photoabsorption spectrum of N_2 molecules, together with the curve fitting results by using Voigt functions. (b) The photoionization spectrum of autoionizing resonance state $(2,0)_n$ of double excited He.

on the electronic and chemical structures of samples grown by laser MBE with high reproducibility. For example, the chemical states and band lineup of heterostructures are characterized by core-level spectroscopy using SX light, confirming the quality of the heterostructures, and then their quantum well (QW) states are investigated by ARPES using VUV light. The "MUSASHI" beamline will be available from mid 2015.

4-3 Science topic: Determination of band diagram for a "*p-n* junction" between Mott insulator $LaMnO_3$ and band insulator Nb:$SrTiO_3$

The perovskite oxide heterojunction, which is composed of two different isostructural materials with a chemical formula of ABO_3, produces distinctive interfacial electronic and/or magnetic properties. These unusual properties have been of considerable interest because of the potential applications of the heterojunction in future electronic devices with multifunctional properties [1]. Extensive studies on the behavior of oxide

heterojunctions have revealed that their novel functionalities, originating from strong electron-electron correlations, can be tuned through interface effects, such as the electric field effect [4-6]. However, in the design of these oxide devices, a fundamental question arises as to whether these interfaces can be described by an analogy to junctions based on conventional semiconductors and/or metals.

The *p-n* junction is one of the most fundamental elements of electronic devices, which have made a great contribution to the development of modern information technology. Thus far, the characteristics of various "*p-n* junctions" based on perovskite oxides have been evaluated [7,8]. Among them, the *p-n* junction composed of the "*p*-type" Mott insulator $LaMnO_3$ (LMO) [9] and the *n*-type oxide semiconductor $SrTiO_3$ (STO) [10] has been intensively studied as a prototypical example [11,12]. Despite the Mott insulating ground states in LMO [13], it has been reported that clear rectification properties of *p-n* junctions are obtained in LMO/Nb:STO heterointerfaces [11,12]. These results suggest that the *p-n* junction characteristics are dominated by the "practical" carrier concentration in LMO and are designed by analogy to conventional semiconductor technology: the carrier density estimated from thermodynamic measurements, such as photocurrent measurement (4×10^{19} cm^{-3} [12]), directly corresponds to the practical carrier concentration N_p in LMO, while one hole per unit cell is expected from the chemical formula (1.7×10^{22} cm^{-3}).

On the other hand, the interfacial properties of the LMO/STO heterointerface exhibit other interesting aspects reflecting its strongly correlated nature. LMO/STO superlattices exhibit ferromagnetic properties appearing at the heterointerface of non-magnetic bulk compounds [14-17]. Therefore, in order to control the junction properties, it is indispensable to determine precisely the interfacial electronic structure; in particular, the band diagram and its dependence on carrier concentration.

For this purpose, we determined the band diagram of LMO/Nb:STO *p-n* junctions and its carrier concentration dependence by using X-ray photoemission spectroscopy (XPS). Figure 4 shows the valence band spectra for the constituent oxides: a thick LMO film (100 ML) and Nb:STO substrates with different Nb concentrations. Extrapolation of the linear portion of the leading edge to the energy axis (the background level) yields a valence band

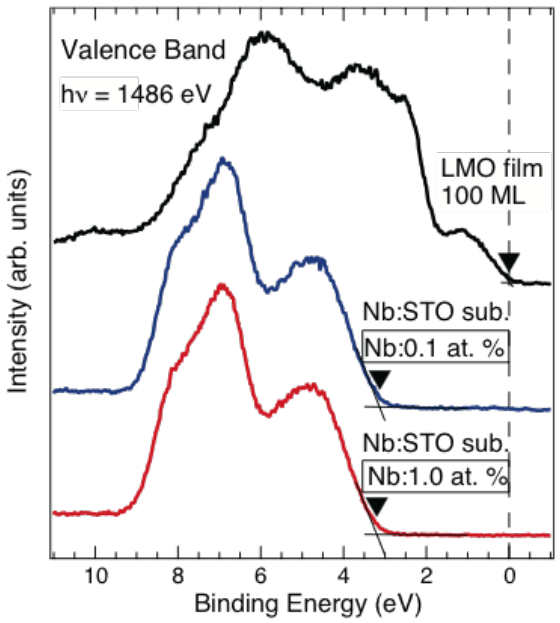

Fig. 4: Valence-band photoemission spectra for the surfaces of the constituent oxides: A 100-ML LMO film, a 0.1 at. % Nb-doped STO substrate, and a 1.0 at. % Nb-doped STO substrate. The triangles indicate the VBM of the respective surfaces, estimated from the intersection point between the extrapolation of the linear portion of the leading edge and the background signal level.

maximum (VBM) for the constituent oxides. The values of VBM were estimated to be –0.02±0.06 eV for the 100-ML LMO films, 3.13±0.05 eV for the 0.1 at. % Nb-doped STO substrates, and 3.20±0.05 eV for the 1.0 at. % Nb-doped STO substrates. Taking into account the band gap of 1.1 eV for LMO [18], the obtained value of VBM suggests that the LMO film can be considered to be a degenerate *p*-type semiconductor without a surface depletion layer. The *p*-type degenerate semiconductive nature of the present LMO film enables us to determine the band lineup more accurately owing to the formation of a flatband at the surface of the LMO film. Meanwhile, the VBM of Nb:STO shows almost the same value of ~3.2 eV between the two substrates, irrespective of their difference in donor concentration. This result is consistent with the fact that STO with a Nb-doping level higher than 0.1 at. % is an *n*-type degenerate semiconductor [19] because the band gap of STO is 3.2±0.1 eV at room temperature [20].

By determining the core-level peak shifts of Nb:STO following the deposition of LMO, we can obtain the amount of band bending (the built-in potential) in the Nb:STO side directly. Figures 5(a) and (b) show the Ti 2*p* core-level spectra of the buried Nb:STO layer for an LMO/Nb:STO junction with a donor concentration of 0.1 at. % and 1.0 at.

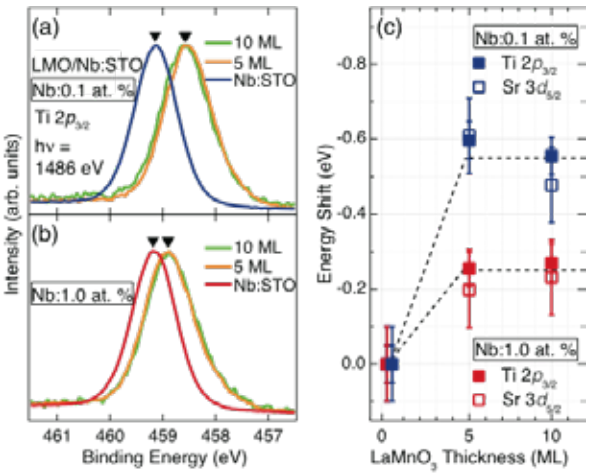

Fig. 5: Shifts of the core level for Nb:STO. Ti 2*p* core-level spectra of (a) 0.1 at. % and (b) 1.0 at. % Nb-doped STO covered by LMO films with various thicknesses. (c) Plot of the energy shifts of the Ti 2*p* and Sr 3*d* core-level peaks as a function of LMO overlayer thickness. The dashed lines are guides for the eye.

%, respectively. For both junctions, a peak shift toward lower binding energies is clearly observed with increasing overlayer LMO thickness and it seems to be saturated at 5-ML LMO deposition. Owing to the short electron escape depth of a few nm in the XPS measurement, the obtained energy shifts of the Ti 2*p* core-level peaks predominantly reflect the potentials in the thin interface region on the Nb:STO side only.

The energy shifts of the Ti 2*p* core-level peaks, as well as those of Sr 3*d,* are summarized in Fig. 5(c). It should be noted that almost the same energy shifts are observed in the Sr 3*d* core-level peaks, indicating that the shifts were caused by the band bending of Nb:STO at the interface with LMO. Considering their saturation levels, the energy shifts can be estimated to be 0.55±0.05 eV for the 0.1 at. % and 0.25±0.05 eV for the 1.0 at. % Nb concentration. Since a flatband is formed at the surface of Nb:STO [19], these shifts directly correspond to the built-in potentials in Nb:STO at the LMO/Nb:STO junctions.

In general, the relationships between the built-in potentials and carrier concentrations for *p*-*n* junctions of conventional semiconductors are given by the following equations [21]:

$$\begin{cases} V_{btot} = V_{bn} + V_{bp} \\ \dfrac{V_{bn}}{V_{bp}} = \dfrac{\varepsilon_p}{\varepsilon_n}\dfrac{N_p}{N_n} \end{cases} \quad (1)$$

Here, V_{btot} is the total built-in potential formed at the interface of the *p*-*n* junction, while V_{bn} and V_{bp} are the potentials distributed on the *n*-type and *p*-type semiconductor sides, correspondingly. N_n (N_p) and ε_n (ε_p) are the donor (acceptor) density and relative permittivity in the *n*-type (*p*-type) semiconductor, respectively. In the present LMO/Nb:STO case, the V_{bn} values of 0.55±0.05 eV for the 0.1 at. % and 0.25±0.05 eV for the 1.0 at. % Nb-doped STO sides are directly determined by XPS measurements. Assuming that (i) V_{btot}, ε_n, ε_p, and N_p remain unchanged for the two heterojunctions with the different Nb-doping concentrations; (ii) N_n and N_p remain unchanged near the boundaries of the junctions; and (iii) the dopant Nb atoms are fully activated in STO (namely, $N_n = 1.7\times10^{19}$ cm^{-3} for the 0.1 at. % and $N_n = 1.7\times10^{20}$ cm^{-3} for the 1.0 at. % Nb-doped STO), the value of V_{btot} can be estimated to be 0.66±0.12 eV from Eqs. (1). The estimated value of V_{btot} is in good agreement with those evaluated from transport measurements, 0.64 eV [11] and 0.77 eV [12]. This agreement suggests that the junction properties of an LMO/Nb:STO heterointerface can be described in the framework of the conventional *p*-*n* junction model [21].

From the values estimated from the conventional *p*-*n* junction model, we deduced the band diagrams of the two LMO/Nb:STO junctions with different donor concentrations, illustrated in Fig. 6. Since the VBM of the present LMO film is located around the Fermi level (see Fig. 4), the flat-band condition may also be fulfilled at the surface of the LMO film. Therefore, the band lineup between the two oxides can be evaluated accurately in the present case. Because Eqs. (1) represent the distribution ratio of V_{btot} between the *n*-type and *p*-type semiconductor sides, the built-in potential on the Nb:STO (LMO) side decreases (increases) from 0.55±0.05 eV (0.11±0.07 eV) to 0.25±0.05 eV (0.41±0.17 eV) by changing the donor concentration in STO from 0.1 at. % to 1.0 at. %. As can be seen in Fig. 6, the donor concentration dependence of the built-in potential formed at the interface between the Mott insulator LMO and the band insulator Nb:STO is well described in the framework of the *p*-*n* junction model for conventional semiconductors: LMO can be regarded as a *p*-type semiconductor with N_p determined from thermodynamic measurements, irrespective of the strongly correlated electron nature of LMO. The present study provides a guideline for the design and control of promising functionalities of heterojunctions based on strongly correlated oxides.

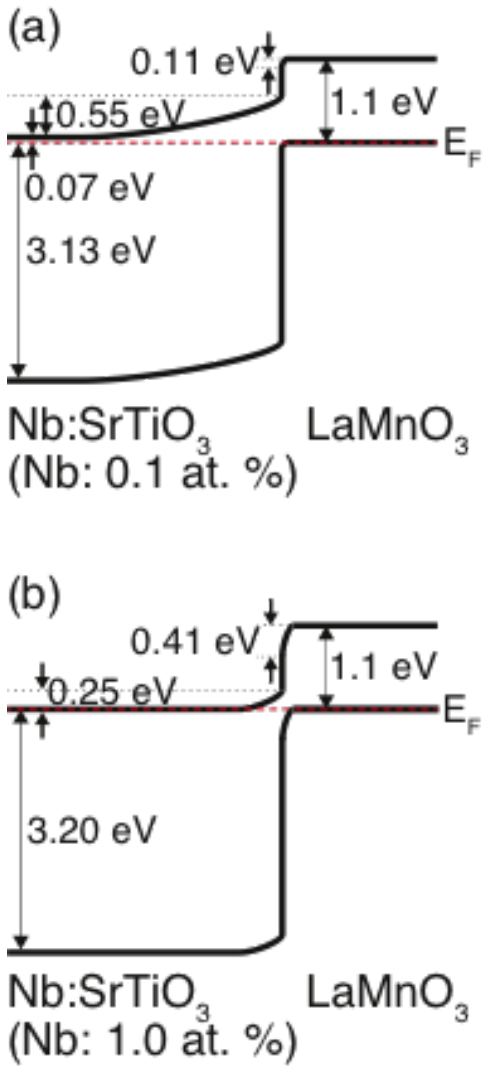

Fig. 6: Band diagrams of LMO/Nb:STO heterojunctions deduced from the present XPS measurements for (a) 0.1 at. % and (b) 1.0 at. % Nb-doped STO. The band gaps of STO and LMO are 3.2 eV [20] and 1.1 eV [18], respectively.

References

[1] H. Y. Hwang, Y. Iwasa, M. Kawasaki, B. Keimer, N. Nagaosa, and Y. Tokura, Nat. Mater. **11**, 103 (2012).

[2] M. Watanabe, A. Toyoshima, Y. Azuma, T. Hayaishi, Y. Yan, and A. Yagishita, Proc. SPIE **3150**, 58 (1997).

[3] http://pfwww.kek.jp/users_info/station_spec/bl28/ bl28a.html

[4] C. H. Ahn, J.-M. Triscone, and J. Mannhart, Nature **424**, 1015 (2003).

[5] M. Nakano, K. Shibuya, D. Okuyama, T. Hatano, S. Ono, M. Kawasaki, Y. Iwasa, and Y. Tokura, Nature **487**, 459 (2012).

[6] A. D. Caviglia, S. Gariglio, N. Reyren, D. Jaccard, T. Schneider, M. Gabay, S. Thiel, G. Hammerl, J. Mannhart, and J.-M. Triscone, Nature **456**, 624 (2008).

[7] H. Tanaka, J. Zhang, and T. Kawai, Phys. Rev. Lett. **88**, 027204 (2002).

[8] A. Sawa, T. Fujii, M. Kawasaki, and Y. Tokura, Appl. Phys. Lett. **86**, 112508 (2005).

[9] J. Töpfer and J. B. Goodenough, J. Solid State Chem. **130**, 117 (1997).

[10] H. P. R. Frederikse and W. R. Hosler, Phy. Rev. **161**, 822 (1967).

[11] M. Nakamura, A. Sawa, J. Fujioka, M. Kawasaki, and Y. Tokura, Phys. Rev. B **82**, 201101 (2010).

[12] J. Fujioka, M. Nakamura, M. Kawasaki, and Y. Tokura, J. Appl. Phys. **111**, 016107 (2012).

[13] M. Imada, A. Fujimori, and Y. Tokura, Rev. Mod. Phys. **70**, 1039 (1998).

[14] J. Garcia-Barriocanal, J. C. Cezar, F. Y. Bruno, P. Thakur, N. B. Brookes, C. Utfeld, A. Rivera-Calzada, S. R. Giblin, J. W. Taylor, J. A. Duffy, S. B. Dugdale, T. Nakamura, K. Kodama, C. Leon, S. Okamoto, and J. Santamaria, Nat. Commun. **1**, 82 (2010).

[15] W. S. Choi, D. W. Jeong, S. S. A. Seo, Y. S. Lee, T. H. Kim, S. Y. Jang, H. N. Lee, and K. Myung-Whun, Phys. Rev. B **83** 195113 (2011).

[16] X. Zhai, C. S. Mohapatra, A. B. Shah, J. M. Zuo, and J. N. Echstein, J. Appl. Phys. **113**, 173913 (2013).

[17] J. Garcia-Barriocanal, F. Y. Bruno, A. Rivera-Calzada, Z. Sefrioui, N. M. Nemes, M. Garcia-Hernández, J. Rubio-Zuazo, G. R. Castro, M. Varela, S. J. Pennycook, C. Leon, and J. Santamaria, Adv. Mater. **22**, 627 (2010).

[18] T. Arima, Y. Tokura, and J. B. Torrance, Phys. Rev. B **48**, 17006 (1993).

[19] M. Minohara, I. Ohkubo, H. Kumigashira, and M. Oshima, Appl. Phys. Lett. **90**, 132123 (2007).

[20] J. A. Noland, Phys. Rev. **94**, 724 (1954).

[21] S. M. Sze and K. K. Ng, Physics of Semiconductor Devices, 3rd ed. (Wiley, Hoboken, NJ, 2007).